Ni anchored to hydrogen-substituted graphdiyne for lithium sulfide cathodes in lithium–sulfur batteries

Louisa C. Greenburg[1], Xin Gao[1], Pu Zhang[1], Xueli Zheng[1,2], Jingyang Wang[1,3], Rafael A. Vilá[1], Yi Cui*[1,2,4]

[1]Department of Materials Science and Engineering, Stanford University, Stanford, CA 94305, USA.

[2]Stanford Institute for Materials and Energy Sciences, SLAC National Accelerator Laboratory, 2575 Sand Hill Road, Menlo Park, CA 94025, USA.

[3]Materials Sciences Division, Lawrence Berkeley National Laboratory, Berkeley, CA 94720, USA.

[4]Department of Energy Science and Engineering, Stanford University, Stanford, CA 94305, USA.

Correspondence and requests for materials should be addressed to Yi Cui (*email: yicui@stanford.edu).

KEYWORDS: Li–S battery, lithium sulfide cathode, Ni catalyst, hydrogen-substituted graphdiyne

ABSTRACT

Lithium–sulfur (Li–S) batteries are promising candidates for next-generation energy storage systems due to their high theoretical energy density and the low cost of sulfur. However, slow conversion kinetics between the insulating S and lithium sulfide (Li_2S) remains as a technical challenge. In this work, we report a catalyst featuring nickel (Ni) single atoms and clusters anchored to a porous hydrogen-substituted graphdiyne support (termed Ni@HGDY), incorporated in Li_2S cathodes. The rapidly synthesized catalyst was found to enhance ionic and electronic conductivity, decrease reaction overpotential, and promote more complete conversion between Li_2S and sulfur. The addition of Ni@HGDY to commercial Li_2S powder enabled a capacity of over 516 mAh $g^{-1}_{Li_2S}$ at 1C for over 125 cycles, whereas the control Li_2S cathode managed to maintain just over 200 mAh $g^{-1}_{Li_2S}$. These findings highlight the efficacy of Ni as a metal catalyst and demonstrate the promise of HGDY in energy storage devices.

The lithium–sulfur (Li–S) battery has emerged as a candidate for next-generation energy storage systems.[1] With a high theoretical energy density (2567 Wh kg^{-1}), Li–S batteries also benefit from sulfur's low-cost and non-toxicity.[1–3] However, several obstacles hinder its commercial viability. First, S and its discharge product lithium sulfide (Li_2S) are poor ion and electron conductors, resulting in slow charge transport and sluggish reaction kinetics, which contribute to lower sulfur utilization and poor cyclability.[4–6] A second issue is that S is denser than Li_2S, leading to volumetric changes in the cathode, mechanical instability, and poor cycle life.[7] Further, lithium polysulfide (LiPS) reaction intermediates dissolve in the electrolyte and shuttle to the anode. This "shuttle effect" contributes to loss of active material and increased internal resistance.[1,8] Various approaches have been implemented to control these issues, including coating sulfur particles to mitigate the shuttle effect[9,10], incorporating conductive or catalytic additives to improve redox kinetics[11], and even engineering void space in the sulfur cathode to allow volume change during cycling.[12–14]

Another strategic approach to accommodate volumetric change is to use Li_2S as the starting cathode material, thus beginning in the most expanded state.[6,15,16] Starting with the discharge product would also allow for anode-free Li–S cells, eliminating extra volume and weight from excess Li.[17] However, the Li_2S cathode requires a significant activation overpotential on the first cycle and suffers from stability issues during long-term cycling, making the Li_2S cathode challenging to execute despite its theoretical advantage.[18] Additionally,

commercially available Li_2S powder consists mostly of micron-sized particles. This larger particle size means ions and electrons have longer paths to travel, compounding issues of poor ion transport and electronic conductivity already inherent to Li_2S and leads to rapid buildup of inactive sulfur species in the cathode.[19]

To address the slow kinetics of the Li–S system, transition metals have been identified as one category of effective catalysts.[20] Previous works on Li–S catalysts have found effective transition metals ranging in size from large nanoparticles[21,22] to atomically dispersed single-atoms.[23–29] Small cluster and single-atom catalysts, however, offer higher atomic and gravimetric efficiencies, and they may display unique selectivity compared to larger particles due to differences in electronic state.[30] These metals catalysts are often bound to carbon supports and are mixed into the cathode active material or coated onto the separator to improve the kinetics in the sulfur cathode. A shortcoming of unmodified carbon supports, such as graphene, is that they do not effectively trap LiPSs to alleviate the shuttle effect due to their non-polarity.[31] Modifications to nonpolar carbon supports, such as heteroatom doping of graphene, can enable significant polysulfide trapping ability[32,33], yet another issue remains; the small pores inherent to the six-membered ring of graphene-derived materials do not facilitate fast ion transport through its planes.[34] For these reasons, we should explore carbon supports that may provide good polysulfide trapping ability while also facilitating fast ion transport.

To that end, we report a catalyst featuring nickel (Ni) supported on hydrogen-substituted graphdiyne, termed Ni@HGDY (**Figure 1**). The HGDY has larger pores (16.3 Å between opposing acetylene linkages) compared to traditional graphene-derived supports, allowing for superior ion transport while also providing good electronic conductivity from its π-conjugated

network.[35] Its high surface area also provides a high density of active centers.[36] Furthermore, previous studies have indicated that the conjugated system of HGDY contributes to polysulfide trapping that would mitigate the shuttle effect.[37,38] Ni has shown great promise as a single-atom catalyst in Li–S batteries in Ni-N_3[39], Ni-N_4[40] and Ni-N_5[41] configurations and as nanoparticles[21,39,42]. Yet, we have seen few Li–S studies featuring Ni clusters or single atoms bound directly to carbon, particularly to HGDY and its acetylene linkages. This Ni-C bond may induce a change in the electronic structure of Ni, its interaction with sulfur species, and its catalytic effect. Additionally, Ni is abundant and lower cost than other catalytic metals such as Co.[43] Using commercial Li_2S powder that received no additional treatment, we fabricated Ni@HGDY/Li_2S cathodes for Li–S batteries. We demonstrate that the Ni@HGDY catalyst improves the redox kinetics of the Li–S system, decreases internal resistance, and reduces loss of active material. With the commercially produced Li_2S and Ni@HGDY catalyst, we maintain a capacity at a 1C current rate of over 516 mAh g^{-1} (based on Li_2S) after 125 cycles, over two times the capacity of the control Li_2S cathode. This work demonstrates the catalytic behavior of Ni bound to HGDY and motivates further exploration of HGDY and its derivatives in Li–S batteries.

To fabricate Ni@HGDY, the porous HGDY aerogel was first synthesized according to a previously reported sol-gel method.[44] Raman spectroscopy was conducted to confirm the successful crosslinking reaction (**Supplementary Figure 1**). The peak at ca. 2208 cm^{-1} suggests the successful formation of acetylenic linkages, while the broad fluorescence peak may be due to

the formation of the large conjugated system, which was reported previously.[44] Broad peaks at ca. 1352 cm^{-1} and ca. 1586 cm^{-1} can be assigned to the D band and G band peaks from the carbon aromatic rings.[45] Scanning electron microscopy (SEM) imaging confirmed the highly porous morphology of HGDY (**Supplementary Figure 2**).

The aerogel was then immersed in a dilute solution of nickel chloride ($NiCl_2$) in ethanol to form solvated Ni precursor on HGDY with a theoretical mass loading of 0.1 wt% Ni compared to the dry aerogel. After evaporation of the solvent, the $NiCl_2$/HGDY aerogel is touched on a hotplate (set to 450°C) in an argon-filled glovebox, and a sparking reaction occurs, yielding Ni@HGDY (**Figure 2a** and **Supplementary Figure 3**). Our previous work suggests this ultrafast sparking synthesis, without further oxidizers, can reach 1600 K in 40 ms.[36] When the aerogel contacts the hot plate, the sparking reaction propagates throughout HGDY, reducing the Ni precursor and releasing chlorine (**Supplementary Figure 4**). The entire aerogel changes from brown to black color upon sparking while preserving its shape. Additionally, scanning electron microscopy (SEM) imaging of Ni@HGDY revealed the aerogel retains its porous structure (**Figure 2b**). No Ni particles were observed during SEM imaging, suggesting dispersed Ni formation.

Ni K-edge X-ray absorption spectroscopy was performed to elucidate the structure of Ni on HGDY. Ni foil and the Ni precursor, $NiCl_2$, were also measured for reference. The X-ray

absorption near-edge structure (XANES) spectra (**Figure 2c**) reveals that the rising edge of Ni@HGDY occurs at an energy between those of Ni foil and $NiCl_2$, suggesting that Ni has an average oxidation state between Ni^0 and Ni^{2+}.[46,47] Extended X-ray absorption fine structure (EXAFS) analysis and subsequent Fourier transform provides insight into the bonding environment of the Ni atoms.[48] The first peak from Ni@HGDY, at 1.29 Å and distinct from peaks in the $NiCl_2$ reference, is likely from the Ni-C bonding of Ni atoms anchored directly on the HGDY carbon aerogel (**Figure 2d**). The second peak at 2.15 Å, approximately the same position as the Ni metal reference, can be attributed to the first shell Ni-Ni interaction.[47] Notably, this second peak is not nearly as significant as would be found in larger particles of metallic Ni.[46] Further, for metallic Ni, we would expect the XANES spectrum to suggest an oxidation state of zero. For example, we found that when increasing the Ni loading, the rising edge matched that of Ni foil (**Supplementary Figure 5a**), and the Ni-Ni interaction became much more pronounced (**Supplementary Figure 5b**). Instead, based on the average Ni oxidation state between zero and 2^+ from XANES, the Ni-C and slight Ni-Ni bonding from EXAFS, and prior literature with similar spectral features further validated by scanning transmission electron microscopy,[49] we believe the Ni@HGDY catalyst consists of small Ni atoms and clusters of few atoms bonded to the

HGDY support. The existence of clusters as opposed to larger nanoparticles is further supported by transmission electron microscopy imaging, during which no Ni particles were clearly observed (**Supplementary Figure 6**).

To further explore the interaction between Ni and HGDY, density functional theory calculations were performed to determine energetically favorable configurations of HGDY anchoring single-atom Ni and Ni clusters of two, three, or four atoms. Single-atom Ni most favorably bonds to two C atoms of an acetylene linkage with an adsorption energy of -2.73 eV (**Figure 2e**). A Ni atom bound to the center of the benzene ring is less favorable thermodynamically, with an adsorption energy of -2.53 eV (**Supplementary Figure 7**). The two-atom and three-atom Ni clusters also most favorably bind to C atoms of the linkages, with a total adsorption energy of -2.78 eV and -2.97 eV respectively (**Supplementary Figure 8** and **Supplementary Figure 9**). These energetically preferred structures demonstrate the effectiveness of the acetylene linkages as binding locations for single-/few-atom Ni. In the most energetically favorable configurations of a four-atom Ni cluster on HGDY, the cluster is bound to both the benzene ring and an acetylene linkage (**Supplementary Figure 10**). The involvement of the benzene ring in the four-atom cluster indicates that the rings may promote larger agglomerations

of Ni, and it is the acetylene linkages that could enable HGDY to favorably stabilize small cluster and single atom Ni, which would translate to more active sites per mass of Ni catalyst.

To prepare the Ni@HGDY catalyst for electrochemical testing, we loaded commercial Li_2S and Ni@HGDY (4:1 mass ratio) onto carbon paper. The X-ray diffraction pattern of the Ni@HGDY/Li_2S cathode clearly confirms the Li_2S on carbon paper (**Supplementary Figure 11a**), while the peaks associated with Ni@HGDY (**Supplementary Figure 11b**) are not clearly observed, likely due in part to the low crystallinity and quantity of Ni@HGDY compared to Li_2S. To isolate the effect of the Ni compared to the HGDY alone, HGDY/Li_2S and control Li_2S cathodes were prepared in a parallel approach. Cathodes were assembled into coin cells with a Li metal anode and conventional electrolyte.

Impedance analysis (**Figure 3a**) shows that the Ni@HGDY/Li_2S cell has the smallest semicircle in the high-frequency region, indicating the least charge transfer resistance[16], followed by HGDY/Li_2S, then the bare Li_2S. We then examined if this improved charge transport may contribute to facilitating the Li_2S oxidation reaction, as a considerable obstacle in operation of Li_2S cathodes is the initial activation required upon the first charge from Li_2S to S_8. This activation is especially challenging with large, bulky Li_2S particles, as found in commercially available Li_2S.

HGDY reduces the overpotential required for initial activation of Li_2S from 3.66 V to 3.53 V vs Li/Li^+ at 0.1 C (**Figure 3b**). The addition of Ni to HGDY further reduces this overpotential to 3.36 V. Ni@HGDY maintains the lowest overpotential throughout this entire first charge activation.

To further clarify the effect of Ni@HGDY in the cathode, a newly assembled Li metal cell with a Li_2S cathode and one with a Ni@HGDY/Li_2S cathode were charged once and disassembled. We then measured sulfur K-edge XANES on the cathodes (**Figure 3c** and **Supplementary Figure 12**). The peaks at 2480 eV and 2485.5 eV can be attributed to the LiTFSI salt.[50] The bare Li_2S cathode shows a shoulder at 2470.5 eV, which is assigned to LiPS and implies incomplete conversion to elemental sulfur.[51] Further, the S_8 peak at around 2472 eV is more prominent in the sample with Ni@HGDY, which also has the concave feature at 2475 eV that is characteristic of S_8.[52] The weaker concavity of this region in the control sample suggests the presence of Li_2S, which can be typically identified by a convex feature at ~ 2476 eV.[52] This result suggests that Ni@HGDY allows for more complete activation and conversion from Li_2S to S_8, likely due to its superior catalytic effect and ion/electron transport. More complete activation and conversion between sulfur species should contribute to higher specific capacity, as observed in in the first charge voltage profile (**Figure 3b**).

Cyclic voltammetry (CV) was employed to examine the effect of Ni@HGDY on the Li–S reaction kinetics. **Figure 3d** shows the cyclic voltammograms of each cell type at 0.2 mV s^{-1} after an initial activation. Two oxidation peaks can be observed. At 2.37 V, Li_2S converts to long-chain polysulfides, which transform to S_8 at 2.43 V. The reduction peaks correspond to the reverse reaction, from reduction of the elemental S_8 back to polysulfide (~2.3 V), and subsequent reduction to Li_2S_2/Li_2S (~2 V). The addition of HGDY leads to a higher current response than the control Li_2S cathode, yet Ni@HGDY/Li_2S shows the greatest current response, which suggests superior redox kinetics.[53,54] Further, the overpotential of each step is lowest in the Ni@HGDY/Li_2S cell (**Supplementary Figure 13**).

The effect of Ni and HGDY on Li^+ diffusion was examined in the Li_2S, HGDY/Li_2S, and Ni@HGDY/Li_2S cells by recording the peak currents in the cyclic voltammograms at varying scan rates, as shown in **Figure 3e** for Ni@HGDY/Li_2S. The peak current, I_p, and square root of scanning rate, $v^{1/2}$, can be related by the Randles-Sevcik equation: $I_p = (2.69 \times 10^5)\,(n^{1.5})(A)(D_{Li^+}^{0.5})(C_{Li^+})(v^{0.5})$, where n is electrons transferred, A is electrode area, and C_{Li+} is Li^+ concentration.[55,56] Changes in slope can be attributed to relative differences in the diffusion coefficient, D_{Li+}. **Figure 3f** shows the linear relationship between I_p and $v^{1/2}$ for the second

oxidation peak, where Ni@HGDY enables the greatest slope. Analysis of all peaks and associated linear fittings (**Supplementary Figure 14**) reveals that Ni@HGDY has the greatest magnitude slope for each peak, indicating faster Li^+ diffusion throughout the reaction. The improved ion transport should contribute to more complete sulfur conversion in the cell as observed in the S K-edge analysis and the current response of the CVs.

To further examine the electrocatalytic ability of Ni@HGDY to facilitate the conversion reaction, we assembled symmetric cells with carbon paper electrodes loaded with either Ni@HGDY or HGDY (**Supplementary Figure 15**). Cyclic voltammograms were collected between -1.4 and 1.4 V at 10 mV s^{-1} with Li_2S_6 (0.5 M) electrolyte. Ni@HGDY enables a higher current response than HGDY, emphasizing that Ni provides higher activity and reversibility for polysulfide conversion. The effect of Ni@HGDY on the nucleation of the Li_2S discharge species is further studied by conducting Li_2S nucleation tests[57]. We found that Ni@HGDY delivers a greater nucleation capacity than HGDY alone (**Supplementary Figure 16**). We expect that Ni can provide more nucleation sites to facilitate conversion to insoluble discharge species.

Shuttle current characterizations[58] were performed to elucidate the ability of Ni@HGDY to trap polysulfides (**Supplementary Figure 17**). We activated HGDY/Li_2S and Ni@HGDY/Li_2S

cathodes in full cells by galvanostatic cycling followed by a potentiostatic hold at 2.3 V. While HGDY has been shown to have considerable polysulfide trapping ability, we found that HGDY alone was insufficient to prevent shuttling. The HGDY cell exhibited a shuttle current of 0.03 mA, and the slight downwards slope may suggest the reduction of polysulfide species at the anode, as has been previously proposed.[58] It's possible that the large pore size of HGDY may lead to a tradeoff between good ion transport and physical blocking of polysulfides. However, the acetylene linkages and high surface area of HGDY[36] should provide plenty of sites to lessen shuttling. Regardless, in the Ni@HGDY cell, the shuttle current was reduced to 0.01 mA with no obvious sloping, highlighting the ability of Ni@HGDY to reduce polysulfide shuttling and active material loss.

To understand the effect of Ni@HGDY on rate performance, we assembled cells for galvanostatic cycling at different C-rates (**Figure 4a**). At 0.1 C, the bare Li_2S cell exhibits an initial discharge capacity of 574.7 mAh $g_{Li_2S}^{-1}$, giving a 49.3% sulfur utilization compared to the theoretical capacity. With Ni@HGDY, the initial discharge capacity jumps to 773.5 mAh g^{-1}, for a 66.4% sulfur utilization. Compared to the bare cell, the Ni@HGDY/Li_2S cell maintains the superior capacity when the rate is increased to 0.2 C, 0.5 C, 1 C, and 2 C.

We also evaluated the cycling stability of each cell type at a current rate of 1 C (**Figure 4b**). After a three-cycle activation at 0.2 C, the Ni@HGDY/Li_2S cell achieves a maximum capacity of

579.8 mAh g^{-1}, compared to 228.9 mAh g^{-1} for the bare Li_2S cell. Notably, the control Li_2S cell reaches a lower capacity than in the rate performance test at 1 C (Figure 4a). We suspect the shorter activation in the 1 C test (three cycles at 0.2 C) leads to lower capacity, whereas the rate test begins with six cycles at 0.1 C then five cycles at 0.2 C, allowing for better activation of Li_2S before the test reaches the 1 C rate. The Ni@HGDY/Li_2S cathode does not suffer from such a drop in capacity, highlighting more effective Li_2S activation in the presence of Ni@HGDY. Further, the Ni@HGDY/Li_2S cell can maintain 92.9% of its initial capacity at 1 C for over 125 cycles. **Figure 4c** shows representative voltage profiles of each cell at cycle 20. The voltage difference between the charge and discharge profiles is 231.2 mV in the bare Li_2S cell and 218.8 mV in the Ni@HGDY/Li_2S cell, where the difference is calculated at half discharge capacity. Thus, Ni@HGDY decreases the reaction overpotential, consistent with the previous CV result.

Impedance analysis of open-circuit full cells after 30 cycles at 1C shows two semicircles in both the bare Li_2S and the Ni@HGDY/Li_2S cells (**Figure 4d**). The high-frequency semicircle in the Ni@HGDY cell is smaller than in the control, indicating lower impedance at the anode/electrolyte interface.[59] Ni@HGDY may more effectively prevent LiPS shuttle and thus have a less insulating anode surface and superior charge transfer across the interface. This hypothesis is

supported by the lower value of the high frequency x-intercept of Ni@HGDY/Li_2S. This value is mainly affected by the bulk electrolyte resistance, which, in Li–S cells, is largely a reflection of the LiPS concentration in the electrolyte.[60] Less LiPS in the electrolyte would lower electrolyte viscosity and the x-intercept. Ni@HGDY also displays a lower charge transfer resistance as indicated by its smaller middle-frequency semicircle compared to that of the bare Li_2S cell, which may have greater buildup of insulating material on the surface of the cathode.[60] This analysis demonstrates that Ni@HGDY improves charge transport and decreases electrolyte and interfacial resistance throughout the cell during cycling.

SEM images of the same cathodes after 30 cycles confirm that without any catalyst, sulfur species agglomerate into large particles, much of which may be inactive due to the insulating nature of sulfur/Li_2S and their bigger size (**Figure 4e**). In the Ni@HGDY/Li_2S cathode, few large particles are observed. Instead, the porous morphology of the Ni@HGDY is preserved and larger sulfur particles are rarely observed. (**Figure 4f**). These observations suggest that the catalyst promotes more uniform nucleation and smaller particle size, contributing to the lower cell impedance and superior electrochemical performance of Li–S cells with Ni@HGDY.

To become commercially viable, Li_2S cathodes with high mass loadings must be developed. To examine the potential of our catalyst with high Li_2S loading, we fabricated carbon paper-supported cathodes made of commercial Li_2S, Ni@HGDY, and carbon black. The loading of Li_2S was 5.5 mg cm^{-2}. After a three-cycle activation at 0.05C, the high mass loading cell could maintain over 500 mAh g^{-1} for at least 35 cycles at 0.1 C (**Supplementary Figure 18**).

As a proof-of-concept, we fabricated anode-free cells with our Ni@HGDY/Li_2S cathodes (**Supplementary Figure 19**). Demonstrated previously by Nanda et al.,[61] we replaced the Li metal anode with Cu foil, removing excess Li. The Ni@HGDY/Li_2S cathode delivered an initial discharge capacity at 0.1 C of 664.9 mAh g^{-1}, compared to 431.6 mAh g^{-1} for the Li_2S control cathode. The Ni@HGDY/Li_2S cathode maintains a capacity at least 160 mAh g^{-1} greater than that of the control throughout cycling at 0.2 C. Even with no modification made to the Cu foil, this decent performance emphasizes the promise of Li_2S cathodes in anode-free cells.

In summary, we have developed a Ni@HGDY catalyst that improves the redox kinetics and cycling performance of Li_2S cathodes. Using sulfur K-edge XAS, we demonstrate that the catalyst greatly improves initial activation and conversion of commercial Li_2S. Electrochemical measurements show that the superior sulfur conversion is maintained at different rates and over

longer cycling periods. With untreated commercial Li_2S powder, the Ni@HGDY/Li_2S cell delivers a capacity of over 516 mAh g^{-1} for over 125 cycles at 1 C. This catalyst additionally facilitates uniform nucleation of Li_2S in the cathode, preventing a high internal resistance from the buildup of large, insulating particles. Our design of a Ni catalyst anchored to HGDY demonstrates a powerful strategy to combine an atomically efficient metal catalyst with a carbon support that emphasizes both strong catalyst anchoring and application-driven features such as polysulfide trapping and superior ion/electron transport.

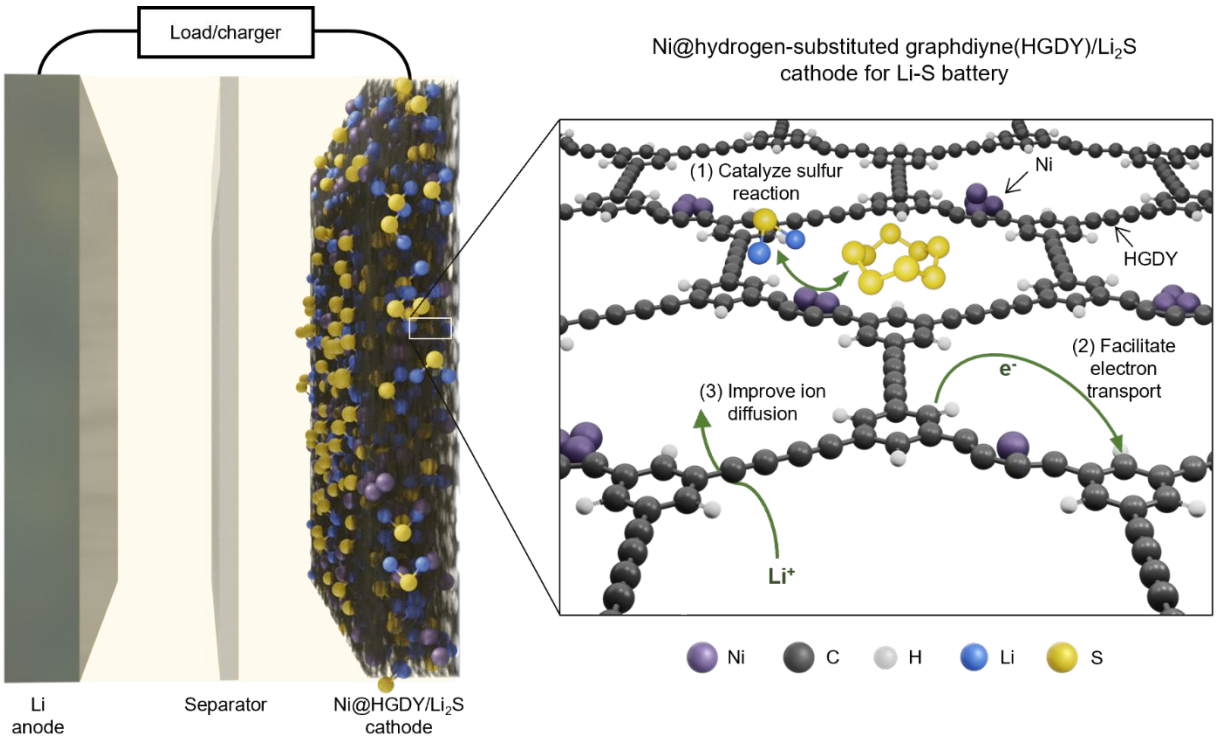

Figure 1. Ni@HGDY catalyst design for Li_2S cathode in Li–S battery. Ni single atoms and clusters are anchored to the HGDY support. The catalyst is mixed with commercial Li_2S powder and improves the kinetics of the Li–S reaction, facilitates electron transport, and improves Li^+ diffusion.

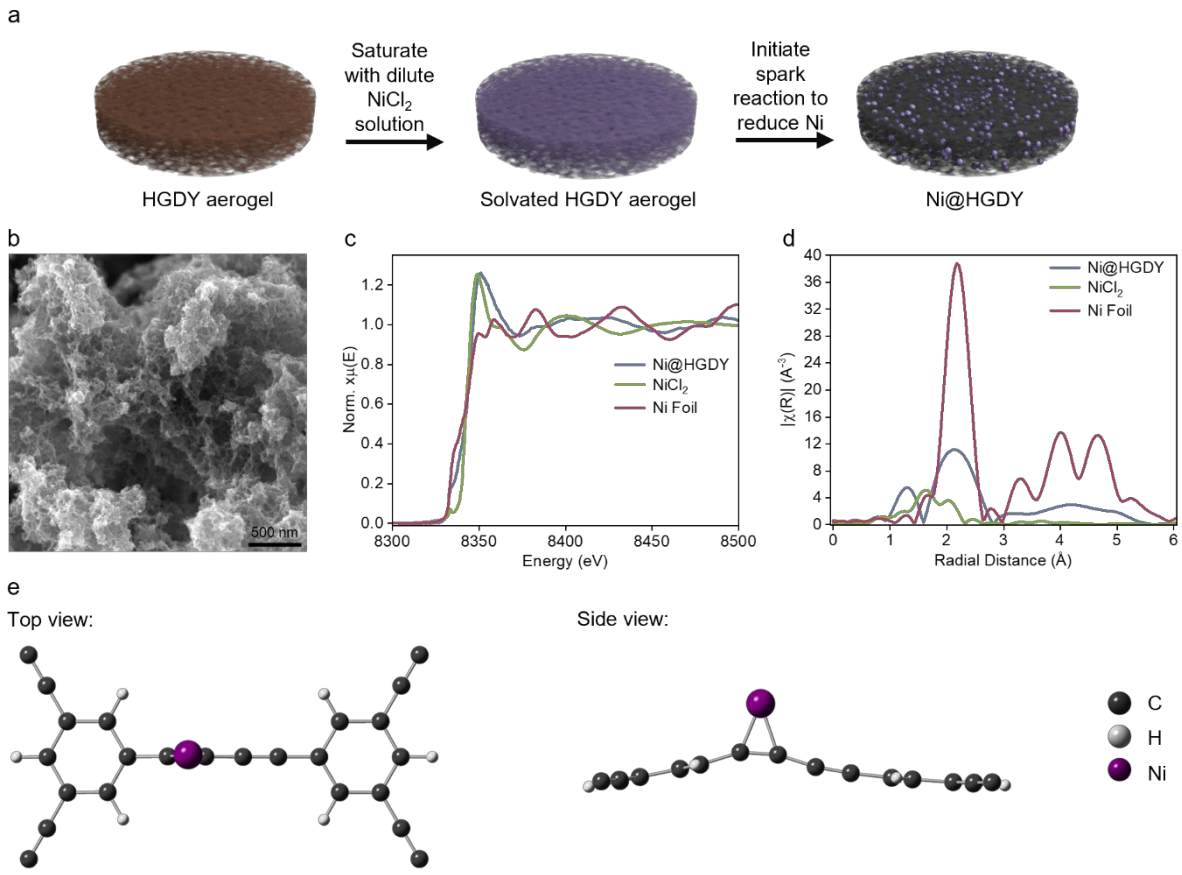

Figure 2: Synthesis and characterization of Ni@HGDY catalyst.

(**a**) Schematic of the Ni@HGDY catalyst preparation, (**b**) SEM image of Ni@HGDY, (**c**) Ni K-edge XANES spectra of Ni@HGDY and $NiCl_2$ and Ni foil references, (**d**) Ni K-edge EXAFS spectra of Ni@HGDY and $NiCl_2$ and Ni foil references, (**e**) Top and side views of the most thermodynamically stable single-atom Ni@HGDY structure as obtained from DFT calculations.

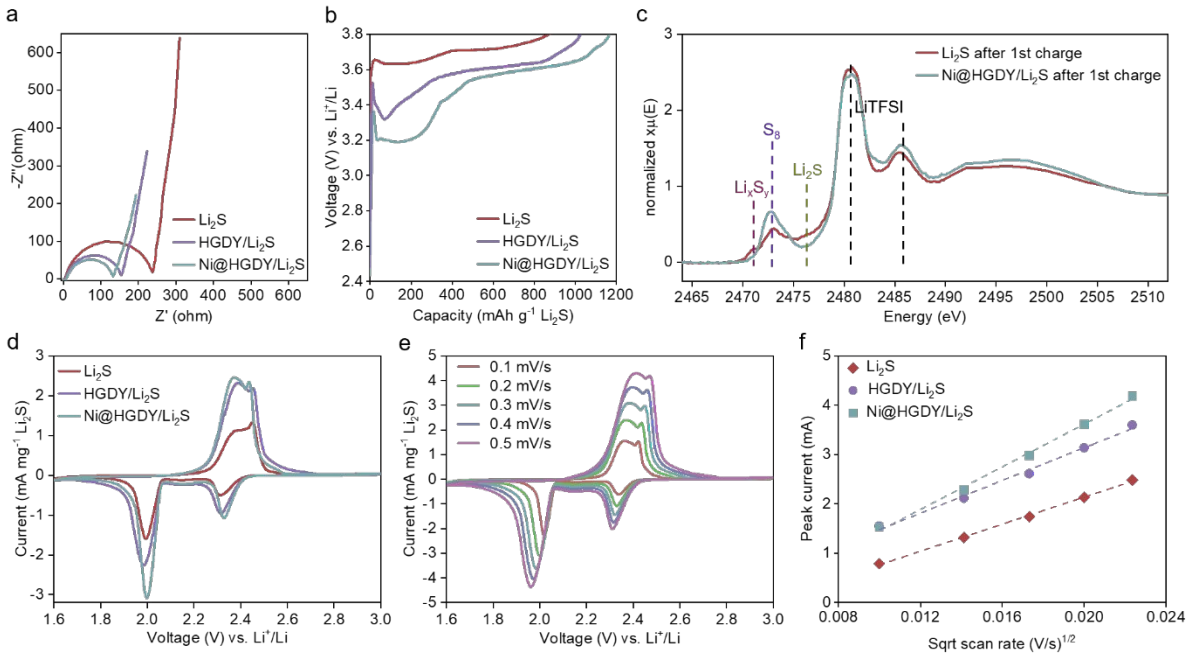

Figure 3: Electrochemical performance of Ni@HGDY/Li_2S cathodes compared to HGDY/Li_2S and bare Li_2S cathodes.

(**a**) Impedance spectra of full cells at open-circuit voltage before cycling, (**b**) first cycle charge profiles at 0.1 C, (**c**) normalized S K-edge spectra after first charge, (**d**) cyclic voltammograms at 0.2 mV s^{-1}, (**e**) cyclic voltammograms of Ni@HGDY/Li_2S full cells at 0.1 mV s^{-1} to 0.5 mV s^{-1}, (**f**) peak current vs. square root of scan rate (filled points) and the associated linear fit (dashed line) of the second oxidation peak.

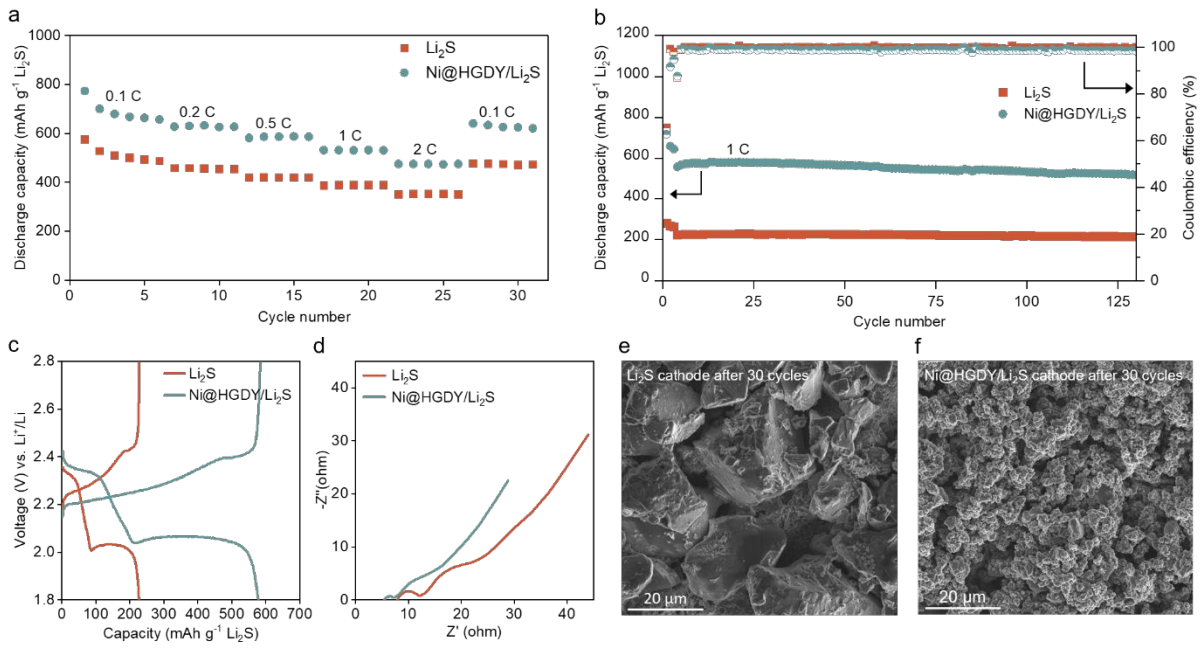

Figure 4. Further electrochemical performance of Ni@HGDY/Li_2S cathodes compared to control Li_2S cathodes.

(**a**) Rate performance of Ni@HGDY and control cells cycled between 1.8 V and 2.8 V at 0.1 C, 0.2 C, 0.5 C, 1 C and 2 C, (**b**) discharge capacity and coulombic efficiency of cells cycled at 1 C after a three-cycle activation at 0.2 C, (**c**) charge-discharge voltage profiles of the 20th cycle at 1 C, (**d**) impedance spectra at open-circuit voltage after 30 cycles, (**e**) SEM image of the Li_2S cathode after 30 cycles, (**f**) SEM image of the Ni@HGDY/Li_2S cathode after 30 cycles.

Acknowledgements

L.C.G. acknowledges support from the National Science Foundation Graduate Research Fellowship under Grant No. 2146755. This work is supported by the U.S. Department of Energy (DOE), under the Assistant Secretary for Energy Efficiency and Renewable Energy, Office of Vehicle Technologies, the Battery Materials Research (BMR) Program, and the Battery500 Consortium, and by the U.S. DOE under the Office of Basic Energy Sciences, Division of Materials Sciences and Engineering (Contract No. DE-AC02-76SF00515). Use of the Stanford Synchrotron Radiation Lightsource, SLAC National Accelerator Laboratory, is supported by the U.S. Department of Energy, Office of Science, Office of Basic Energy Sciences under Contract No. DE-AC02-76SF00515. We thank Dr. Johanna Nelson Weker and Dr. Sharon Bone for the helpful discussion of the XAS data analysis. Part of this work was performed at the Stanford Nano Shared Facilities (SNSF), supported by the National Science Foundation under award ECCS-2026822.

Supporting Information

This Supporting Information is available free of charge at http://pubs.acs.org.

- Details about the experimental and computational methods, Raman spectrum and SEM of HGDY, photos of sparking reaction, X-ray photoelectron spectroscopy spectra demonstrating completion of sparking reaction, XAS of Ni on HGDY with higher Ni concentration, TEM of Ni@HGDY, optimized structures of Ni atom(s) bonded to HGDY, XRD of Ni@HGDY/Li_2S, electrochemical performance, and high mass loading and anode-free cell performance.

References

(1) Manthiram, A.; Fu, Y.; Su, Y.-S. Challenges and Prospects of Lithium–Sulfur Batteries. *Acc. Chem. Res.* **2013**, *46* (5), 1125–1134. https://doi.org/10.1021/ar300179v.

(2) Zhou, G.; Chen, H.; Cui, Y. Formulating Energy Density for Designing Practical Lithium–Sulfur Batteries. *Nat Energy* **2022**, *7* (4), 312–319. https://doi.org/10.1038/s41560-022-01001-0.

(3) Evers, S.; Nazar, L. F. New Approaches for High Energy Density Lithium–Sulfur Battery Cathodes. *Acc. Chem. Res.* **2013**, *46* (5), 1135–1143. https://doi.org/10.1021/ar3001348.

(4) Ji, X.; Nazar, L. F. Advances in Li–S Batteries. *J. Mater. Chem.* **2010**, *20* (44), 9821. https://doi.org/10.1039/b925751a.

(5) Choi, Y.-J.; Chung, Y.-D.; Baek, C.-Y.; Kim, K.-W.; Ahn, H.-J.; Ahn, J.-H. Effects of Carbon Coating on the Electrochemical Properties of Sulfur Cathode for Lithium/Sulfur Cell. *Journal of Power Sources* **2008**, *184* (2), 548–552. https://doi.org/10.1016/j.jpowsour.2008.02.053.

(6) Son, Y.; Lee, J.-S.; Son, Y.; Jang, J.-H.; Cho, J. Recent Advances in Lithium Sulfide Cathode Materials and Their Use in Lithium Sulfur Batteries. *Adv. Energy Mater.* **2015**, *5* (16), 1500110. https://doi.org/10.1002/aenm.201500110.

(7) Yin, Y.-X.; Xin, S.; Guo, Y.-G.; Wan, L.-J. Lithium-Sulfur Batteries: Electrochemistry, Materials, and Prospects. *Angew. Chem. Int. Ed.* **2013**, *52* (50), 13186–13200. https://doi.org/10.1002/anie.201304762.

(8) Ji, X.; Lee, K. T.; Nazar, L. F. A Highly Ordered Nanostructured Carbon–Sulphur Cathode for Lithium–Sulphur Batteries. *Nature Mater* **2009**, *8* (6), 500–506. https://doi.org/10.1038/nmat2460.
(9) Yang, Y.; Yu, G.; Cha, J. J.; Wu, H.; Vosgueritchian, M.; Yao, Y.; Bao, Z.; Cui, Y. Improving the Performance of Lithium–Sulfur Batteries by Conductive Polymer Coating. *ACS Nano* **2011**, *5* (11), 9187–9193. https://doi.org/10.1021/nn203436j.
(10) Wang, H.; Yang, Y.; Liang, Y.; Robinson, J. T.; Li, Y.; Jackson, A.; Cui, Y.; Dai, H. Graphene-Wrapped Sulfur Particles as a Rechargeable Lithium–Sulfur Battery Cathode Material with High Capacity and Cycling Stability. *Nano Lett.* **2011**, *11* (7), 2644–2647. https://doi.org/10.1021/nl200658a.
(11) Ye, H.; Lee, J. Y. Solid Additives for Improving the Performance of Sulfur Cathodes in Lithium–Sulfur Batteries—Adsorbents, Mediators, and Catalysts. *Small Methods* **2020**, *4* (6), 1900864. https://doi.org/10.1002/smtd.201900864.
(12) Wei Seh, Z.; Li, W.; Cha, J. J.; Zheng, G.; Yang, Y.; McDowell, M. T.; Hsu, P.-C.; Cui, Y. Sulphur–TiO2 Yolk–Shell Nanoarchitecture with Internal Void Space for Long-Cycle Lithium–Sulphur Batteries. *Nat Commun* **2013**, *4* (1), 1331. https://doi.org/10.1038/ncomms2327.
(13) Li, W.; Zheng, G.; Yang, Y.; Seh, Z. W.; Liu, N.; Cui, Y. High-Performance Hollow Sulfur Nanostructured Battery Cathode through a Scalable, Room Temperature, One-Step, Bottom-up Approach. *PNAS* **2013**, *110* (18), 7148–7153. https://doi.org/10.1073/pnas.1220992110.
(14) Zhou, W.; Yu, Y.; Chen, H.; DiSalvo, F. J.; Abruña, H. D. Yolk–Shell Structure of Polyaniline-Coated Sulfur for Lithium–Sulfur Batteries. *J. Am. Chem. Soc.* **2013**, *135* (44), 16736–16743. https://doi.org/10.1021/ja409508q.
(15) Yang, Y.; McDowell, M. T.; Jackson, A.; Cha, J. J.; Hong, S. S.; Cui, Y. New Nanostructured Li_2S/Silicon Rechargeable Battery with High Specific Energy. *Nano Lett.* **2010**, *10* (4), 1486–1491. https://doi.org/10.1021/nl100504q.
(16) Seh, Z. W.; Yu, J. H.; Li, W.; Hsu, P.-C.; Wang, H.; Sun, Y.; Yao, H.; Zhang, Q.; Cui, Y. Two-Dimensional Layered Transition Metal Disulphides for Effective Encapsulation of High-Capacity Lithium Sulphide Cathodes. *Nat Commun* **2014**, *5* (1), 5017. https://doi.org/10.1038/ncomms6017.
(17) Weber, R.; Genovese, M.; Louli, A. J.; Hames, S.; Martin, C.; Hill, I. G.; Dahn, J. R. Long Cycle Life and Dendrite-Free Lithium Morphology in Anode-Free Lithium Pouch Cells Enabled by a Dual-Salt Liquid Electrolyte. *Nat Energy* **2019**, *4* (8), 683–689. https://doi.org/10.1038/s41560-019-0428-9.
(18) Yang, Y.; Zheng, G.; Misra, S.; Nelson, J.; Toney, M. F.; Cui, Y. High-Capacity Micrometer-Sized Li_2S Particles as Cathode Materials for Advanced Rechargeable Lithium-Ion Batteries. *J. Am. Chem. Soc.* **2012**, *134* (37), 15387–15394. https://doi.org/10.1021/ja3052206.
(19) Chen, H.; Wang, C.; Dong, W.; Lu, W.; Du, Z.; Chen, L. Monodispersed Sulfur Nanoparticles for Lithium–Sulfur Batteries with Theoretical Performance. *Nano Lett.* **2015**, *15* (1), 798–802. https://doi.org/10.1021/nl504963e.
(20) Li, Y.-J.; Fan, J.-M.; Zheng, M.-S.; Dong, Q.-F. A Novel Synergistic Composite with Multi-Functional Effects for High-Performance Li–S Batteries. *Energy Environ. Sci.* **2016**, *9* (6), 1998–2004. https://doi.org/10.1039/C6EE00104A.

(21) Mosavati, N.; Chitturi, V. R.; Arava, L. M. R.; Salley, S. O.; Ng, K. Y. S. Effects of Nickel Particle Size and Graphene Support on the Electrochemical Performance of Lithium/Dissolved Polysulfide Batteries. *Electrochimica Acta* **2015**, *185*, 297–303. https://doi.org/10.1016/j.electacta.2015.10.061.
(22) Zhang, Z.; Kong, L.-L.; Liu, S.; Li, G.-R.; Gao, X.-P. A High-Efficiency Sulfur/Carbon Composite Based on 3D Graphene Nanosheet@Carbon Nanotube Matrix as Cathode for Lithium-Sulfur Battery. *Adv. Energy Mater.* **2017**, *7* (11), 1602543. https://doi.org/10.1002/aenm.201602543.
(23) Du, Z.; Chen, X.; Hu, W.; Chuang, C.; Xie, S.; Hu, A.; Yan, W.; Kong, X.; Wu, X.; Ji, H.; Wan, L.-J. Cobalt in Nitrogen-Doped Graphene as Single-Atom Catalyst for High-Sulfur Content Lithium–Sulfur Batteries. *J. Am. Chem. Soc.* **2019**, *141* (9), 3977–3985. https://doi.org/10.1021/jacs.8b12973.
(24) Zhang, K.; Chen, Z.; Ning, R.; Xi, S.; Tang, W.; Du, Y.; Liu, C.; Ren, Z.; Chi, X.; Bai, M.; Shen, C.; Li, X.; Wang, X.; Zhao, X.; Leng, K.; Pennycook, S. J.; Li, H.; Xu, H.; Loh, K. P.; Xie, K. Single-Atom Coated Separator for Robust Lithium–Sulfur Batteries. *ACS Appl. Mater. Interfaces* **2019**, *11* (28), 25147–25154. https://doi.org/10.1021/acsami.9b05628.
(25) Zhao, H.; Tian, B.; Su, C.; Li, Y. Single-Atom Iron and Doped Sulfur Improve the Catalysis of Polysulfide Conversion for Obtaining High-Performance Lithium–Sulfur Batteries. *ACS Appl. Mater. Interfaces* **2021**, *13* (6), 7171–7177. https://doi.org/10.1021/acsami.0c20446.
(26) Wang, F.; Li, J.; Zhao, J.; Yang, Y.; Su, C.; Zhong, Y. L.; Yang, Q.-H.; Lu, J. Single-Atom Electrocatalysts for Lithium Sulfur Batteries: Progress, Opportunities, and Challenges. *ACS Materials Lett.* **2020**, *2* (11), 1450–1463. https://doi.org/10.1021/acsmaterialslett.0c00396.
(27) Han, X.; Zhang, Z.; Xu, X. Single Atom Catalysts Supported on N-Doped Graphene toward Fast Kinetics in Li–S Batteries: A Theoretical Study. *J. Mater. Chem. A* **2021**, *9* (20), 12225–12235. https://doi.org/10.1039/D1TA01948A.
(28) Andritsos, E. I.; Lekakou, C.; Cai, Q. Single-Atom Catalysts as Promising Cathode Materials for Lithium–Sulfur Batteries. *J. Phys. Chem. C* **2021**, *125* (33), 18108–18118. https://doi.org/10.1021/acs.jpcc.1c04491.
(29) Liang, Z.; Shen, J.; Xu, X.; Li, F.; Liu, J.; Yuan, B.; Yu, Y.; Zhu, M. Advances in the Development of Single-Atom Catalysts for High-Energy-Density Lithium-Sulfur Batteries. *Advanced Materials n/a* (n/a), 2200102. https://doi.org/10.1002/adma.202200102.
(30) Liu, L.; Corma, A. Metal Catalysts for Heterogeneous Catalysis: From Single Atoms to Nanoclusters and Nanoparticles. *Chem. Rev.* **2018**, *118* (10), 4981–5079. https://doi.org/10.1021/acs.chemrev.7b00776.
(31) Zheng, G.; Zhang, Q.; Cha, J. J.; Yang, Y.; Li, W.; Seh, Z. W.; Cui, Y. Amphiphilic Surface Modification of Hollow Carbon Nanofibers for Improved Cycle Life of Lithium Sulfur Batteries. *Nano Lett.* **2013**, *13* (3), 1265–1270. https://doi.org/10.1021/nl304795g.
(32) Liu, C.-Y.; Li, E. Y. Adsorption Mechanisms of Lithium Polysulfides on Graphene-Based Interlayers in Lithium Sulfur Batteries. *ACS Appl. Energy Mater.* **2018**, *1* (2), 455–463. https://doi.org/10.1021/acsaem.7b00096.
(33) Hou, T.-Z.; Chen, X.; Peng, H.-J.; Huang, J.-Q.; Li, B.-Q.; Zhang, Q.; Li, B. Design Principles for Heteroatom-Doped Nanocarbon to Achieve Strong Anchoring of Polysulfides for Lithium-Sulfur Batteries. *Small* **2016**, *12* (24), 3283–3291. https://doi.org/10.1002/smll.201600809.

(34) Yao, F.; Güneş, F.; Ta, H. Q.; Lee, S. M.; Chae, S. J.; Sheem, K. Y.; Cojocaru, C. S.; Xie, S. S.; Lee, Y. H. Diffusion Mechanism of Lithium Ion through Basal Plane of Layered Graphene. *J. Am. Chem. Soc.* **2012**, *134* (20), 8646–8654. https://doi.org/10.1021/ja301586m.

(35) He, J.; Wang, N.; Cui, Z.; Du, H.; Fu, L.; Huang, C.; Yang, Z.; Shen, X.; Yi, Y.; Tu, Z.; Li, Y. Hydrogen Substituted Graphdiyne as Carbon-Rich Flexible Electrode for Lithium and Sodium Ion Batteries. *Nat Commun* **2017**, *8* (1), 1172. https://doi.org/10.1038/s41467-017-01202-2.

(36) Zheng, X.; Gao, X.; Vilá, R. A.; Jiang, Y.; Wang, J.; Xu, R.; Zhang, R.; Xiao, X.; Zhang, P.; Greenburg, L. C.; Yang, Y.; Xin, H. L.; Zheng, X.; Cui, Y. Hydrogen-Substituted Graphdiyne-Assisted Ultrafast Sparking Synthesis of Metastable Nanomaterials. *Nat. Nanotechnol.* **2022**. https://doi.org/10.1038/s41565-022-01272-4.

(37) Wang, Y.; He, J.; Zhang, Z.; Liu, Z.; Huang, C.; Jin, Y. Graphdiyne-Modified Polyimide Separator: A Polysulfide-Immobilizing Net Hinders the Shuttling of Polysulfides in Lithium–Sulfur Battery. *ACS Appl. Mater. Interfaces* **2019**, *11* (39), 35738–35745. https://doi.org/10.1021/acsami.9b11989.

(38) Kong, S.; Cai, D.; Li, G.; Xu, X.; Zhou, S.; Ding, X.; Zhang, Y.; Yang, S.; Zhou, X.; Nie, H.; Huang, S.; Peng, P.; Yang, Z. Hydrogen-Substituted Graphdiyne/Graphene as an Sp/Sp ^{2} Hybridized Carbon Interlayer for Lithium–Sulfur Batteries. *Nanoscale* **2021**, *13* (6), 3817–3826. https://doi.org/10.1039/D0NR07878F.

(39) Pei, H.; Yang, Q.; Yu, J.; Song, H.; Zhao, S.; Waterhouse, G. I. N.; Guo, J.; Lu, S. Self-Supporting Carbon Nanofibers with Ni-Single-Atoms and Uniformly Dispersed Ni-Nanoparticles as Scalable Multifunctional Hosts for High Energy Density Lithium-Sulfur Batteries. *Small* **2022**, *18* (27), 2202037. https://doi.org/10.1002/smll.202202037.

(40) Ma, Y.; Wu, T.; Jiao, Y.; Wang, F.; Chen, B.; Yan, Y.; Hu, A.; Li, Y.; Fan, Y.; He, M.; Hu, Y.; Li, Y.; Lei, T.; Zhang, Y.; Chen, W.; Huang, M.; Zhu, J.; Li, F. Single Nickel Atom Catalysts Enable Fast Polysulfide Redox for Safe and Long-Cycle Lithium–Sulfur Batteries. *Small* **2022**, *18* (51), 2205470. https://doi.org/10.1002/smll.202205470.

(41) Zhang, S.; Ao, X.; Huang, J.; Wei, B.; Zhai, Y.; Zhai, D.; Deng, W.; Su, C.; Wang, D.; Li, Y. Isolated Single-Atom Ni–N5 Catalytic Site in Hollow Porous Carbon Capsules for Efficient Lithium–Sulfur Batteries. *Nano Lett.* **2021**. https://doi.org/10.1021/acs.nanolett.1c03499.

(42) Tsao, Y.; Gong, H.; Chen, S.; Chen, G.; Liu, Y.; Gao, T. Z.; Cui, Y.; Bao, Z. A Nickel-Decorated Carbon Flower/Sulfur Cathode for Lean-Electrolyte Lithium–Sulfur Batteries. *Adv. Energy Mater.* **2021**, *11* (36), 2101449. https://doi.org/10.1002/aenm.202101449.

(43) Li, W.; Erickson, E. M.; Manthiram, A. High-Nickel Layered Oxide Cathodes for Lithium-Based Automotive Batteries. *Nat Energy* **2020**, *5* (1), 26–34. https://doi.org/10.1038/s41560-019-0513-0.

(44) Du, R.; Zhang, N.; Xu, H.; Mao, N.; Duan, W.; Wang, J.; Zhao, Q.; Liu, Z.; Zhang, J. CMP Aerogels: Ultrahigh-Surface-Area Carbon-Based Monolithic Materials with Superb Sorption Performance. *Adv. Mater.* **2014**, *26* (47), 8053–8058. https://doi.org/10.1002/adma.201403058.

(45) Yang, Q.; Guo, Y.; Gu, J.; Li, N.; Wang, C.; Liu, Z.; Li, X.; Huang, Z.; Wei, S.; Xu, S.; Song, L.; Fan, J.; Chen, Z.; Qiu, J.; Zhi, C. Scalable Synthesis of 2D Hydrogen-Substituted

Graphdiyne on Zn Substrate for High-Yield N2 Fixation. *Nano Energy* **2020**, *78*, 105283. https://doi.org/10.1016/j.nanoen.2020.105283.
(46) Zhao, C.; Dai, X.; Yao, T.; Chen, W.; Wang, X.; Wang, J.; Yang, J.; Wei, S.; Wu, Y.; Li, Y. Ionic Exchange of Metal–Organic Frameworks to Access Single Nickel Sites for Efficient Electroreduction of CO_2. *J. Am. Chem. Soc.* **2017**, *139* (24), 8078–8081. https://doi.org/10.1021/jacs.7b02736.
(47) Yang, H.; Lin, Q.; Zhang, C.; Yu, X.; Cheng, Z.; Li, G.; Hu, Q.; Ren, X.; Zhang, Q.; Liu, J.; He, C. Carbon Dioxide Electroreduction on Single-Atom Nickel Decorated Carbon Membranes with Industry Compatible Current Densities. *Nat Commun* **2020**, *11* (1), 593. https://doi.org/10.1038/s41467-020-14402-0.
(48) Ren, W.; Tan, X.; Jia, C.; Krammer, A.; Sun, Q.; Qu, J.; Smith, S. C.; Schueler, A.; Hu, X.; Zhao, C. Electronic Regulation of Nickel Single Atoms by Confined Nickel Nanoparticles for Energy-Efficient CO_2 Electroreduction. *Angew Chem Int Ed* **2022**, *61* (26). https://doi.org/10.1002/anie.202203335.
(49) Jiang, K.; Siahrostami, S.; Zheng, T.; Hu, Y.; Hwang, S.; Stavitski, E.; Peng, Y.; Dynes, J.; Gangisetty, M.; Su, D.; Attenkofer, K.; Wang, H. Isolated Ni Single Atoms in Graphene Nanosheets for High-Performance CO_2 Reduction. *Energy Environ. Sci.* **2018**, *11* (4), 893–903. https://doi.org/10.1039/C7EE03245E.
(50) Zhang, L.; Ling, M.; Feng, J.; Mai, L.; Liu, G.; Guo, J. The Synergetic Interaction between LiNO3 and Lithium Polysulfides for Suppressing Shuttle Effect of Lithium-Sulfur Batteries. *Energy Storage Materials* **2018**, *11*, 24–29. https://doi.org/10.1016/j.ensm.2017.09.001.
(51) Cuisinier, M.; Cabelguen, P.-E.; Evers, S.; He, G.; Kolbeck, M.; Garsuch, A.; Bolin, T.; Balasubramanian, M.; Nazar, L. F. Sulfur Speciation in Li–S Batteries Determined by Operando X-Ray Absorption Spectroscopy. *J. Phys. Chem. Lett.* **2013**, *4* (19), 3227–3232. https://doi.org/10.1021/jz401763d.
(52) Gorlin, Y.; Patel, M. U. M.; Freiberg, A.; He, Q.; Piana, M.; Tromp, M.; Gasteiger, H. A. Understanding the Charging Mechanism of Lithium-Sulfur Batteries Using Spatially Resolved Operando X-Ray Absorption Spectroscopy. *J. Electrochem. Soc.* **2016**, *163* (6), A930–A939. https://doi.org/10.1149/2.0631606jes.
(53) Zhou, G.; Pei, S.; Li, L.; Wang, D.-W.; Wang, S.; Huang, K.; Yin, L.-C.; Li, F.; Cheng, H.-M. A Graphene-Pure-Sulfur Sandwich Structure for Ultrafast, Long-Life Lithium-Sulfur Batteries. *Adv. Mater.* **2014**, *26* (4), 625–631. https://doi.org/10.1002/adma.201302877.
(54) Li, M.; Zhou, J.; Zhou, J.; Guo, C.; Han, Y.; Zhu, Y.; Wang, G.; Qian, Y. Ultrathin SnS 2 Nanosheets as Robust Polysulfides Immobilizers for High Performance Lithium-Sulfur Batteries. *Materials Research Bulletin* **2017**, *96*, 509–515. https://doi.org/10.1016/j.materresbull.2017.05.016.
(55) Zhou, G.; Tian, H.; Jin, Y.; Tao, X.; Liu, B.; Zhang, R.; Seh, Z. W.; Zhuo, D.; Liu, Y.; Sun, J.; Zhao, J.; Zu, C.; Wu, D. S.; Zhang, Q.; Cui, Y. Catalytic Oxidation of Li_2S on the Surface of Metal Sulfides for Li−S Batteries. *Proc Natl Acad Sci USA* **2017**, *114* (5), 840–845. https://doi.org/10.1073/pnas.1615837114.
(56) Zhao, Z.; Pathak, R.; Wang, X.; Yang, Z.; Li, H.; Qiao, Q. Sulfiphilic FeP/RGO as a Highly Efficient Sulfur Host for Propelling Redox Kinetics toward Stable Lithium-Sulfur Battery. *Electrochimica Acta* **2020**, *364*, 137117. https://doi.org/10.1016/j.electacta.2020.137117.

(57) Fan, F. Y.; Carter, W. C.; Chiang, Y.-M. Mechanism and Kinetics of Li2S Precipitation in Lithium–Sulfur Batteries. *Advanced Materials* **2015**, *27* (35), 5203–5209. https://doi.org/10.1002/adma.201501559.
(58) Moy, D.; Manivannan, A.; Narayanan, S. R. Direct Measurement of Polysulfide Shuttle Current: A Window into Understanding the Performance of Lithium-Sulfur Cells. *J. Electrochem. Soc.* **2015**, *162* (1), A1–A7. https://doi.org/10.1149/2.0181501jes.
(59) Peled, E.; Goor, M.; Schektman, I.; Mukra, T.; Shoval, Y.; Golodnitsky, D. The Effect of Binders on the Performance and Degradation of the Lithium/Sulfur Battery Assembled in the Discharged State. *J. Electrochem. Soc.* **2017**, *164* (1), A5001–A5007. https://doi.org/10.1149/2.0161701jes.
(60) Waluś, S.; Barchasz, C.; Bouchet, R.; Alloin, F. Electrochemical Impedance Spectroscopy Study of Lithium–Sulfur Batteries: Useful Technique to Reveal the Li/S Electrochemical Mechanism. *Electrochimica Acta* **2020**, *359*, 136944. https://doi.org/10.1016/j.electacta.2020.136944.
(61) Nanda, S.; Gupta, A.; Manthiram, A. A Lithium–Sulfur Cell Based on Reversible Lithium Deposition from a Li_2S Cathode Host onto a Hostless-Anode Substrate. *Adv. Energy Mater.* **2018**, *8* (25), 1801556. https://doi.org/10.1002/aenm.201801556.

TOC Graphic

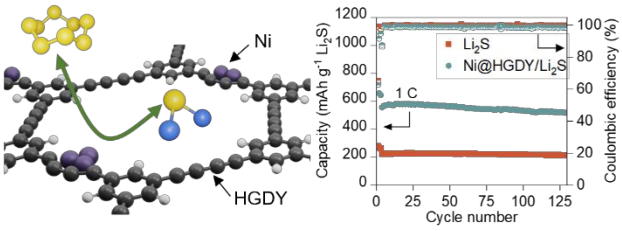

Ni@hydrogen-substituted graphdiyne (Ni@HGDY) catalyst for Li_2S cathodes